

Determination of the stress field in the Kopeh Dagh and Eastern Iran regions

Ghasem Ghorbani ROSTAM 

Department of physics, College of Basic Sciences, Islamshahr branch,
Islamic Azad University, Tehran, Iran; e-mail: gh_gh_r@yahoo.com

Abstract: The land of Iran is situated in a compression zone with a high seismicity rate due to the convergence of Arabian and Eurasian plates. In this study, the stress field of two provinces of Kopeh Dagh and Eastern Iran, which are located in the east and northeast of Iran, has been studied and compared. These two provinces are different in terms of seismicity patterns so that Kopeh Dagh is much more active than Eastern Iran. To achieve this goal, the iterative joint inversion method for stress and fault orientations developed by *Vavryčuk (2014)* has been used. The average direction of the maximum principal stress (σ_1) and the maximum horizontal stress (SHmax) in the study area are estimated to be N30.1°E and N12.1°E, respectively. These directions are in agreement with the convergence of the Arabian plate and the Eurasian plate. The value of the optimal friction coefficient was determined for both regions and it was found that this coefficient is lower in Kopeh Dagh than in Eastern Iran. This indicates a potential relationship of the fault friction with the activity pattern and seismicity of in the region.

Key words: tectonic stress, earthquake, focal mechanism, inversion, Kopeh Dagh, Eastern Iran

1. Introduction

As a result of the collision of the Arabian plate (south and southwest of Iran) and the Eurasian plate (north and northeast of Iran), important tectonic provinces have emerged. *Mirzaei et al. (1998)* have considered five tectonic provinces for Iran, including: (1) the continental–continental collision zone of Zagros in southwest Iran, (2) highly seismic regions of Alborz–Azarbayegan covering north and northwest of Iran, which constitute a part of northern limit of the Alpine–Himalayan orogenic belt, (3) the intraplate environment of Central–East Iran, (4) the continental collision zone of Kopeh Dagh in northeast, and (5) the oceanic–continental subduction zone of Makran in southeast (Fig. 1). These tectonic provinces have repeatedly experienced devastating earthquakes. The Alborz mountain range zone is a folded and faulted system in the north of Iran, with

a current northwest convergence rate of 8 mm/yr (Vernant *et al.*, 2004). Fault strike in this region varies from N110°E in the west to N80°E in the east. Zagros is an active zone where more than 50% of Iran's earthquakes recorded by the global networks have occurred (Mirzaei *et al.*, 1998). There is a sizeable reduction in the seismicity rate from Zagros in the west to the Makran subduction zone in the east. The Central Iran zone is surrounded by western Afghanistan to the east, which is considered as seismically stable being crossed by north–south right lateral faults distributed over 400 km (Walker and Jackson, 2004). Extensive studies have been conducted in these provinces. These studies include GPS measurements (e.g., Vernant *et al.*, 2004; Bayer *et al.*, 2006; Masson *et al.*, 2007; Walker *et al.*, 2021); seismological (e.g., Yamini-Fard and Hatzfeld, 2008; Yamini-Fard *et al.*, 2007; Kouhpeyma *et al.*, 2021), tectonic (e.g., Tchalenko, 1975; Molinaro *et al.*, 2004; Regard *et al.*, 2004, 2010), and stratigraphic studies (e.g., Alavi, 1996; Leturmy and Robin, 2010). In previous studies, the determination of the

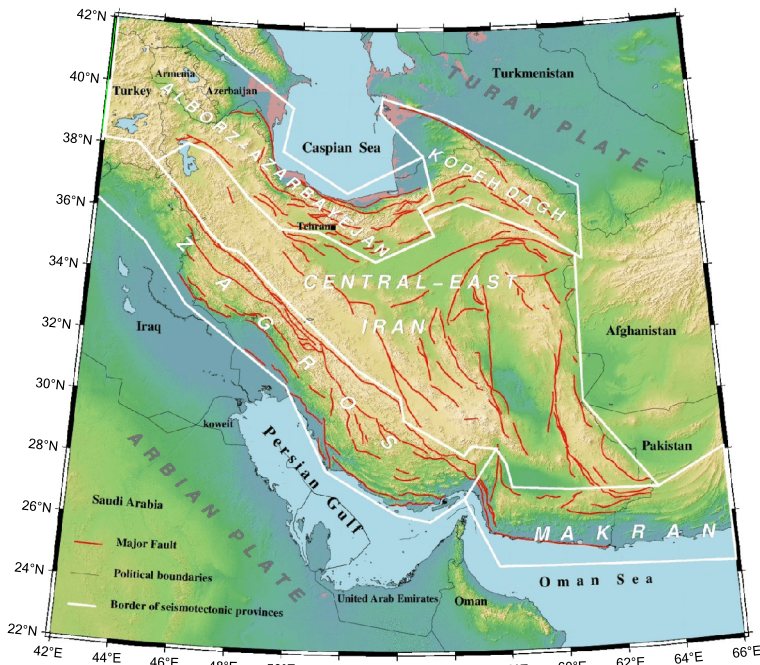


Fig. 1. Seismotectonic provinces of Iran based on Mirzaei *et al.* (1998).

stress field of two tectonic seismic provinces of Kopeh Dagh and eastern Iran has received less attention.

One of the methods of determining the stress field is the inversion of focal mechanisms proposed and developed by *Michael (1984)* and *Vavryčuk (2014)*. *Bott (1959)* explained that slip on each fault plane occurs in the direction of the maximum shear stress. *Carey and Brunier (1974)* applied the Bott criterion to the stress inversion assuming that movement represented by strains or slickenside due to slip of the fault plane is created by a single common tensor. Their analysis was further extended and modified by many other researchers (e.g., *Angelier, 1979; Etchecopar et al., 1981; Armijo et al., 1982; Michael, 1984; Reches, 1987; Angelier, 1990*) and applied later to inverting for stress from focal mechanisms. The Michael's inversion is based on the assumption that the direction of the tangential traction on the plane tends to be parallel to the slip direction. In the iterative joint inversion method (*Vavryčuk, 2014*), the constraint of fault instability is applied to the Michael's method (*Michael, 1984*).

In this paper, we collect focal mechanisms of earthquakes in the Kopeh Dagh and Eastern Iran regions from the Global Centroid Moment Tensor (GCMT) catalogue and we invert them for the stress field. We apply the above-mentioned method of *Vavryčuk (2014)* to invert for the stress directions, the shape ratio and the friction coefficient in the regions under study and we interpret the obtained results.

2. Seismotectonic of the Kopeh Dagh and Eastern Iran regions

Kopeh Dagh is bounded on the north by the Turan plateau in Eurasia, on the south by Central Iran, on the west by the Alborz-Azerbaijan province, and on the east by the Iran-Afghanistan border. Central-East Iran is bounded on the north by Kopeh Dagh and Alborz, on the south by Makran, on the east by the Zagros, and on the west by Pakistan and Afghanistan. Recent GPS measurements indicate that Arabia moves approximately northwards, with respect to Eurasia, at $\sim 23 \text{ mma}^{-1}$ (e.g., *McClusky et al., 2003; Vernant et al., 2004*). The northward motion of Arabia is partly accommodated by subduction beneath the Makran (*Vernant et al., 2004*), with the remainder accommodated by shortening in the Kopeh Dagh and Binalud ranges of NE

Iran. Shortening north of the Zagros requires N–S right-lateral strike-slip faulting between Central Iran and stable Afghanistan. This is observed in the N–S right-lateral fault systems on either side of the Lut desert, in east Iran (e.g., *Walker and Jackson, 2004; Hollingsworth et al., 2006*). Eastern Iran is moving north to the Eurasian plate at a rate of approximately 13 mma^{-1} ; while this value decreases to 7 mma^{-1} between the Eastern Iran and the Arabia plate (*Vernant and Chéry, 2006*).

The Eastern Iran is characterized by a scattered seismic activity with large magnitude earthquakes, long recurrence periods and seismic gaps along several Quaternary faults (*Hamzehloo, 2005*). The seismicity map of Kopeh Dagh and East of Iran from 2000 to 2020 is presented in Fig. 2. These earthquakes are generally shallow and are usually associated with surface faulting. More than 95% of the earthquakes in the study area occurred at a depth of less than 20 km (see Fig. 3).

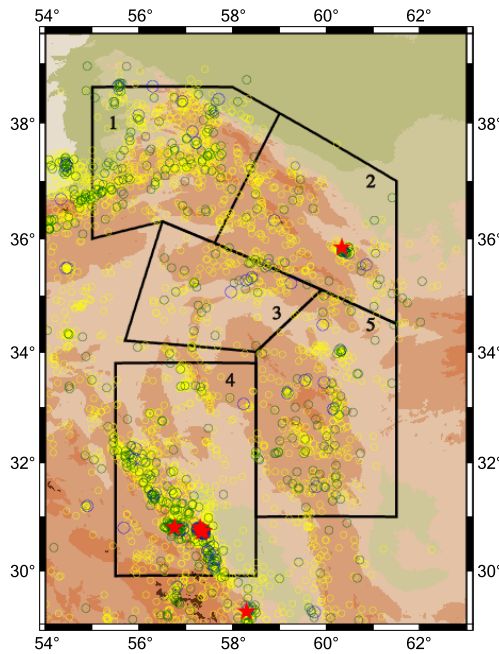


Fig. 2. Seismicity map of Kopeh Dagh and Eastern Iran from 2000 to 2020. Epicentres of earthquakes are marked by circles and stars. The epicentres are colour-coded according to the local magnitude ML. Yellow circles: $3 \leq \text{ML} < 4$, green circles: $4 \leq \text{ML} < 5$, blue circles: $5 \leq \text{ML} < 6$, red stars: $\text{ML} \geq 6$.

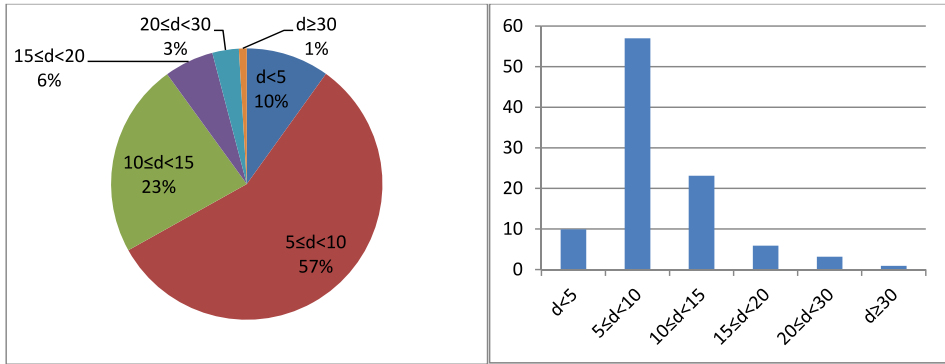


Fig. 3. The Pie and bar chart for the percentage of earthquake depths (in km).

3. Methodology

The tectonic stress is characterized by directions of the principal stresses σ_1 , σ_2 and σ_3 , where $\sigma_3 \leq \sigma_2 \leq \sigma_1$, and by the so-called shape ratio: $R = (\sigma_1 - \sigma_2) / (\sigma_1 - \sigma_3)$. Analysis of the stress field was carried out by many researchers (e.g., *Angelier, 1979; Etchecopar et al., 1981; Armijo et al., 1982; Michael, 1984; Reches, 1987; Angelier, 1990*) and applied for determining stress from focal mechanisms. However, the inversion for stress from focal mechanisms is not straightforward. Focal mechanisms provide us with orientations of two nodal planes but without knowing which nodal plane is the fault and which is the auxiliary plane corresponding to the slip vector. This knowledge is, however, important and confusion of the fault and the auxiliary plane can produce errors in the stress inversion. In order to identify the true fault planes, *Lund and Slunga (1999)* used the constraint of fault instability in the stress inversion of *Gephart and Forsyth (1984)* and improved its performance. In the iterative joint inversion method (*Vavryčuk, 2014*), the same constraint is applied to the Michael’s method (*Michael, 1984*).

Vavryčuk (2014) demonstrated that the Michael’s method is capable to obtain the principal stress direction accurately even without knowledge of the true fault planes, but the shape ratio R is calculated with a large error. If the fault planes are identified using the fault instability constraint, this difficulty is removed. In addition, his numerical tests show that the iterative

stress inversion is fast and accurate and performs much better than the standard linear inversion of *Michael (1984)*.

The Michael's inversion is based on the assumption that the direction of the tangential traction on the plane tends to be parallel to the slip direction:

$$\hat{\tau} = \frac{\vec{\tau}(\hat{n}, \sigma)}{|\vec{\tau}(\hat{n}, \sigma)|} = \hat{s}, \quad (1)$$

where $\vec{\tau}(\hat{n}, \sigma)$ is the tangential traction component on the fault plane with unit normal vector \hat{n} , due to the deviatoric stress tensor σ . Vector $\hat{\tau}$ is the unit vector associated with $\vec{\tau}$ and vector \hat{s} is the direction of the slip vector. A single fault cannot completely constrain the deviatoric stress tensor. Thus, Eq. (1) should be solved for a set of faults so that a single σ that best satisfies all of the faults is found. The tangential traction component is obtained by the following equation:

$$\vec{\tau} = \sigma \hat{n} - [(\sigma \hat{n}) \cdot \hat{n}] \hat{n}. \quad (2)$$

Since this method cannot determine absolute stress values, $|\vec{\tau}|$ is equated to 1 in Eq. (2). The assumption of the zero isotropic stress is applied, because the method is not capable to retrieve the trace of the stress tensor. Considering this assumption, we can write the system of equations for the stress tensor components, which can be solved by the standard method of least squares. By finding the stress tensor, we can obtain the principal stresses and their directions.

In order to solve Eq. (2), we need the fault normal \hat{n} . Consequently, we have to identify for each focal mechanisms, which of two nodal planes is the fault. Generally, it is expected that the fault plane is a plane that is more unstable in a given stress field (*Vavryčuk, 2011*). This plane can be recognized in the Mohr circle diagram as the plane satisfying the Mohr-Coulomb criterion. Since the shape ratio R is sufficient to form a three-dimensional Mohr circle diagram without scaling (*Gephart and Forsyth, 1984*), the nodal planes can be located in the Mohr diagram and the nodal plane which has the highest instability for all values of the friction coefficient can be identified.

The iterative joint inversion uses the following equation for the fault instability (*Vavryčuk et al., 2013*):

$$I = \frac{\tau - \mu(\sigma - 1)}{\mu + \sqrt{1 + \mu^2}}, \quad (3)$$

where

$$\sigma = n_1^2 + (1 - 2R)n_2^2 - n_3^2, \quad (4)$$

$$\tau = \sqrt{n_1^2 + (1 - 2R)n_2^2 + n_3^2 - [n_1^2 + (1 - 2R)n_2^2 + n_3^2]^2}. \quad (5)$$

The values of the fault instability are ranging from zero (maximum stability) to one (minimum stability). In Eq. (3), we use various values of friction coefficient μ ranging from 0.2 to 1.2. The optimum friction corresponds to the maximum instability and it is used in the final stress inversion.

In the iterative joint inversion for stress and fault orientations, Michael's method is first applied in a standard way without considering any constraint and with no knowledge of the orientation of the fault planes. After finding the principal stress directions and the shape ratio, these values are used for evaluating the instability of the nodal planes using Eq. (3) for all inverted focal mechanisms. The fault planes are the nodal planes that are more unstable. The orientations of the fault planes found in the first iteration are used in the second iteration performed again, using the Michael's method. The procedure is repeated until the stress converges to some optimum values.

4. Focal mechanism inversion

According to the distribution of earthquakes in the study area and to maintain the condition of stress field homogeneity, we consider 5 sub-regions, for which the stress field is evaluated (Fig. 4). Kopeh Dagh was divided into two parts, east and west (zones 1 and 2) and Eastern Iran was divided into three parts (zones 3, 4, and 5). The map of the studied events and the number of zones are shown in Figure 4. According to this figure, the highest and lowest numbers of data are related to zones 4 (with 41 focal mechanisms) and zones 2 and 3 (with 12 focal mechanisms), respectively. The focal mechanisms are listed in Appendix.

The stress field of each zone was calculated by using the iterative joint inversion of *Vavryčuk (2014)* described in the previous section. The results are summarized in Table 1 and shown in Fig. 5. In addition, the shape ratio

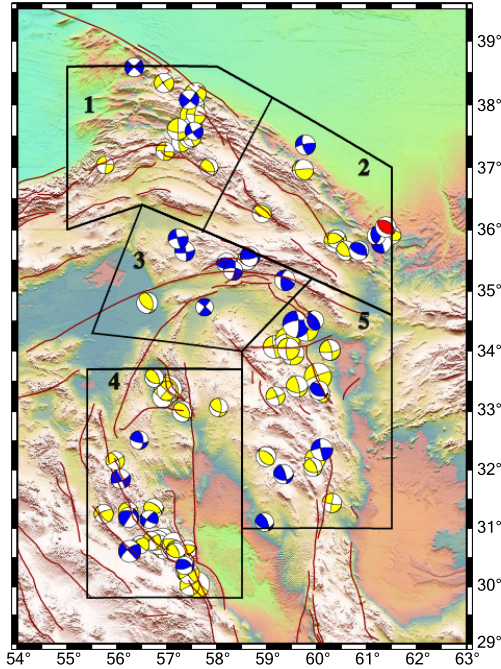


Fig. 4. The study area divided into 5 zones and focal mechanisms of earthquakes in individual zones. The focal mechanisms are color-coded according to depth (yellow: 0–15 km; blue: 15–30 km; red: more than 430 km).

R , the friction coefficient μ , and the maximum horizontal stress SH_{max} are determined for each zone. The direction of the maximum principal stress σ_1 varies from 22.0° (202.0°) in zone 2 to 41.5° (221.5°) in zone 3. The average azimuth of the maximum principal stress in all 5 zones is equal to 30.1° (210.1°). The average directions of σ_2 and σ_3 are equal to 123.7° (303.7°) and 116.0° (296.0°), respectively. The maximum horizontal stress SH_{max} is in the range of 4.4° (zone 1) to 21.4° (zone 5) and their average is 12.1° .

The maximum and minimum shape ratios are 0.68 (zone 2) and 0.88 (zone 5), respectively. The histograms of the shape ratio of all 5 zones are shown in Figure 6. The distribution of the shape ratio values in zones 2 and 3 is broader than in the other zones. The lowest scatter the shape ratio values are observed in zone 4. The scattering of the shape ratio values seems to be inversely proportional to the number of data used in this study. The

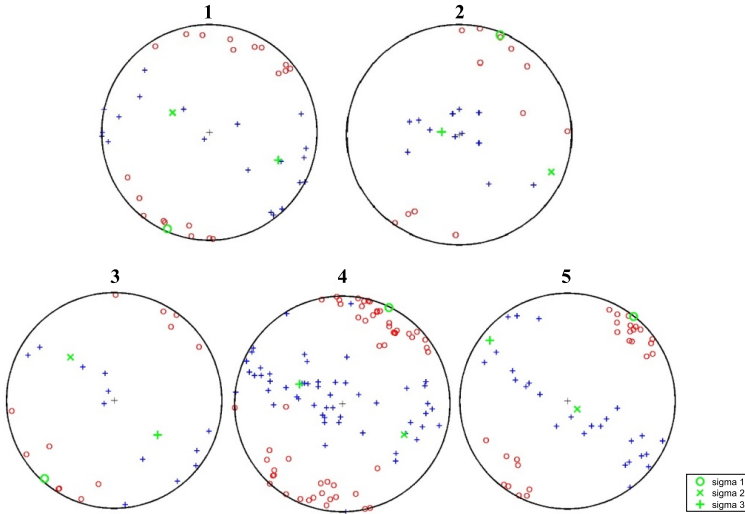


Fig. 5. Focal spheres showing the pressure/tension (P/T) axes of the focal mechanisms together with the principal stress directions. The red circles and blue plus signs mark the P and T axes, respectively. The green circles, crosses and plus signs represent the directions of σ_1 , σ_2 and σ_3 , respectively.

Table 1. The results of the iterative joint inversion for 5 zones. SHmax: maximum horizontal stress, μ : friction coefficient, R : shape ratio, az: azimuth, pl: plunge.

Zone number	Number of focal mechanisms	SHmax (°)	μ	R	σ_1		σ_2		σ_3	
					az (°)	pl (°)	az (°)	pl (°)	az (°)	pl (°)
1	21	4.44	0.30	0.83	203.20	2.10	302.12	76.70	112.71	13.13
2	12	6.41	0.45	0.68	21.99	2.82	112.61	12.44	97.23	77.23
3	12	14.62	0.55	0.87	41.51	4.73	137.19	50.04	307.59	39.56
4	41	13.50	0.70	0.86	25.84	0.86	116.47	36.01	294.65	53.98
5	20	21.44	0.55	0.88	38.05	0.38	130.27	80.39	307.98	9.60

Mohr circle diagram and the confidence level of the principal stress axes are shown for all five zones in Fig. 7.

The fault instability condition was applied with different values of the friction coefficient ranging from 0.20 to 1.00 in 0.05 steps for each event. Then the fault instability for each zone was obtained by averaging, and the maximum value of the fault instability was determined (Table 2). The fric-

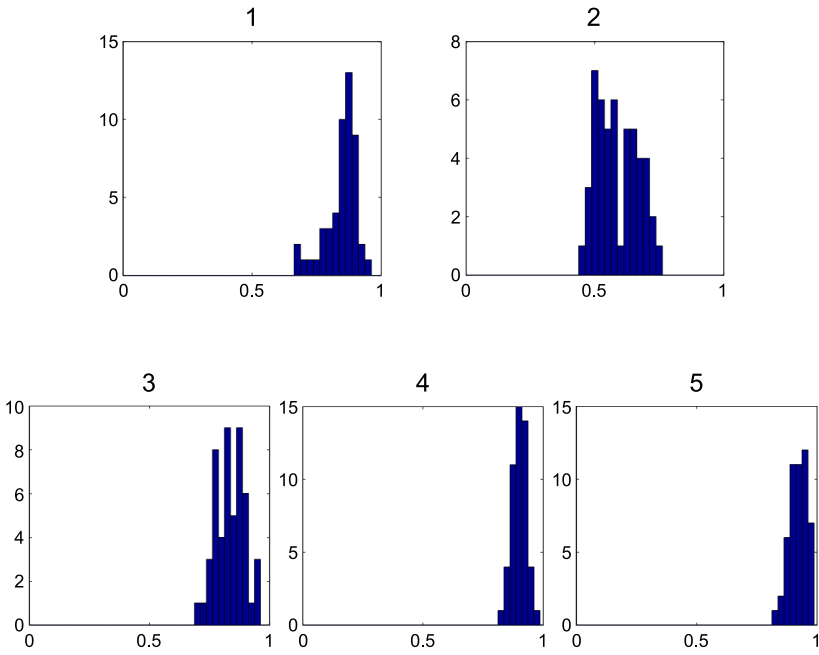


Fig. 6. Histograms of the shape ratio R for 5 zones under study. The zone number is specified on top of each histogram.

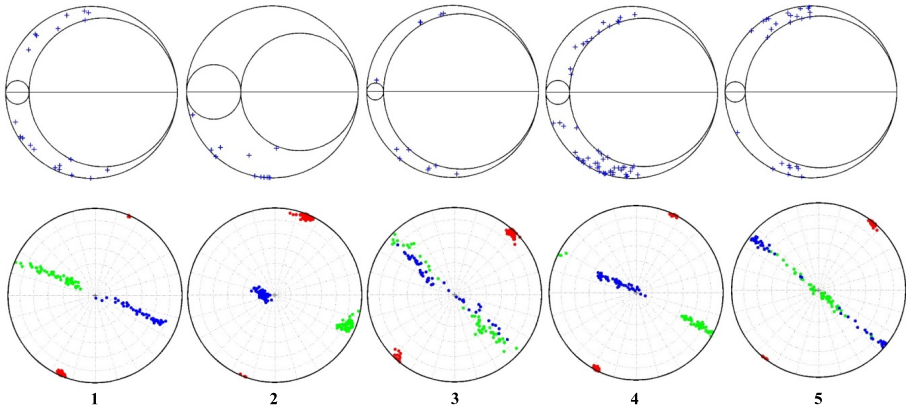


Fig. 7. Mohr circle diagrams (top). Confidence limits of the principal stress axes (bottom). Red (σ_1), green (σ_2), blue (σ_3).

tion coefficient, which produces the highest fault instability in each zone, was considered to be optimum. The averages of the instability in 5 zones based on various friction coefficients are presented in Table 2 and the maximum instability values are highlighted. The maximum and minimum coefficients of friction are 0.70 (zone 4) and 0.30 (zone 1), respectively. In order to better present the dependence of the instability on the friction coefficient and the optimal choice of this coefficient, the scatter chart is drawn in Fig. 8. The instability value is in the range from 0.80 to 0.95. The maximum values are indicated by the red stars. These values occur in zones 1 to 5 for friction coefficients of 0.30, 0.45, 0.55, 0.70 and 0.55, respectively.

Table 2. Average of the fault instability in 5 zones based on varying friction coefficients. The maximum instability values are highlighted.

Friction coefficient	Zone 1	Zone 2	Zone 3	Zone 4	Zone 5
0.20	0.866	0.925	0.845	0.854	0.904
0.25	0.866	0.931	0.827	0.867	0.919
0.30	0.889	0.934	0.881	0.903	0.880
0.35	0.867	0.936	0.888	0.879	0.892
0.40	0.874	0.936	0.847	0.893	0.892
0.45	0.880	0.939	0.847	0.896	0.890
0.50	0.837	0.938	0.846	0.909	0.888
0.55	0.874	0.935	0.908	0.910	0.920
0.60	0.839	0.931	0.844	0.909	0.917
0.65	0.839	0.928	0.906	0.911	0.913
0.70	0.838	0.928	0.904	0.936	0.883
0.75	0.837	0.924	0.901	0.934	0.870
0.80	0.836	0.920	0.899	0.932	0.865
0.85	0.834	0.915	0.896	0.930	0.870
0.90	0.831	0.911	0.893	0.927	0.865
0.95	0.799	0.906	0.890	0.924	0.888
1.00	0.797	0.887	0.887	0.921	0.856

5. Discussion and conclusion

In this study, the iterative stress inversion of focal mechanisms developed by *Vavryčuk (2014)* was applied to determine tectonic stress. The study

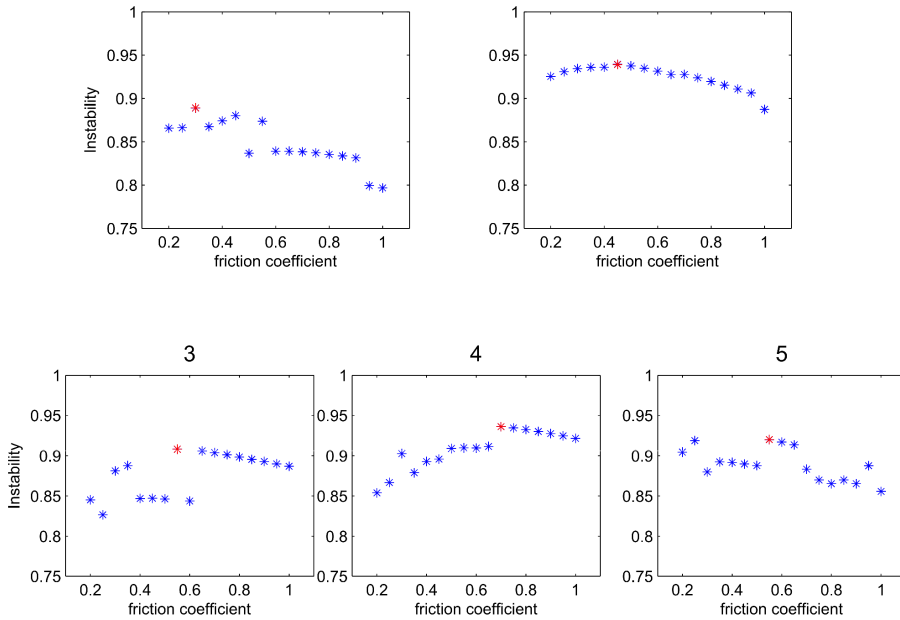


Fig. 8. Diagrams of the fault instability for 5 zones. The maximum instability values are marked by red stars. The zone number is specified on top of each diagram.

area covers two important tectonic provinces in the north and northeast of Iran. The area is divided into 5 zones: zones 1 and 2 are located in the Kopeh Dagh, which is characterized by a relatively high seismicity rate. By contrast, zones 3, 4, and 5 are located in central and eastern Iran, which are characterized by a relatively low seismicity rate.

The direction of the maximum principal stress σ_1 is northeast-southwest, i.e. in the range of 22.0° to 41.5° . This direction is in accordance with the convergence of the Arabian plate in the southwest of Iran and the Eurasian plate in the north of Iran. Also, the direction of the maximum horizontal stress, which is estimated to be 12.1° on average, is consistent with these results.

The shape ratio R in Kopeh Dagh (zones 1 and 2) is lower than in Eastern Iran (zones 3, 4, and 5). This seems to be a reason for a different character of the stress field of these tectonic provinces. Also, zones 1 and 2 differ in the shape ratio R . Therefore, dividing the study area into several smaller zones seems to be logical and necessary.

Another quantity that clearly indicates significant differences between the two provinces of Kopeh Dagh and Eastern Iran is the coefficient of friction. As stated, this coefficient is determined by the instability condition. The value of this coefficient in Kopeh Dagh is lower than that in Eastern Iran. We can speculate that it can be a reason for a higher rate of seismicity in Kopeh Dagh than Eastern Iran. The highest amount of friction coefficient is related to zone 4, which is characterized by the lowest seismicity compared to the other regions of Iran.

Acknowledgements. The stress inversion was performed using the public-open Matlab code STRESSINVERSE developed by *Vavryčuk (2014)* available at <http://www.ig.cas.cz/stress-inverse>.

References

- Alavi M., 1996: Tectonostratigraphic synthesis and structural style of the Alborz mountain system in northern Iran. *J. Geodyn.*, **21**, 1, 1–33, doi: 10.1016/0264-3707(95)00009-7.
- Angelier J., 1979: Determination of the mean principal directions of stresses for a given fault population. *Tectonophysics*, **56**, 3-4, T17–T26, doi: 10.1016/0040-1951(79)90081-7.
- Angelier J., 1990: Inversion of field data in fault tectonics to obtain the regional stress: III. A new rapid direct inversion method by analytical means. *Geophys. J. Int.*, **103**, 2, 363–376, doi: 10.1111/j.1365-246X.1990.tb01777.x.
- Armijo R., Carey E., Cisternas A., 1982: The inverse problem in microtectonics and the separation of tectonic phases. *Tectonophysics*, **82**, 1-2, 145–160, doi: 10.1016/0040-1951(82)90092-0.
- Bayer R., Chery J., Tatar M., Vernant Ph., Abbassi M., Masson F., Nilforoushan F., Doerflinger E., Regard V., Bellier O., 2006: Active deformation in Zagros-Makran transition zone inferred from GPS measurements. *Geophys. J. Int.*, **165**, 1, 373–381, doi: 10.1111/j.1365-246X.2006.02906.x.
- Bott M. H. P., 1959: The mechanics of oblique slip faulting. *Geol. Mag.*, **96**, 2, 109–117, doi: 10.1017/S0016756800059987.
- Carey E., Brunier B., 1974: Analyse théorique et numérique d'un modèle mécanique élémentaire appliqué à l'étude d'une population de failles. *C. R. Acad. Sci. Paris*, **279**, D, 891–894 (in French).
- Etchecopar A., Vasseur G., Daignieres M., 1981: An inverse problem in microtectonics for the determination of stress tensors from fault striation analysis. *J. Struct. Geol.*, **3**, 1, 51–65, doi: 10.1016/0191-8141(81)90056-0.
- Gephart J. W., Forsyth D. W., 1984: An improved method for determining the regional stress tensor using earthquake focal mechanism data: Application to the San Fernando Earthquake Sequence. *J. Geophys. Res. Solid Earth*, **89**, B11, 9305–9320,

- doi: 10.1029/JB089iB11p09305.
- Hamzehloo H., 2005: Determination of causative fault parameters for some recent Iranian earthquakes using near field SH-wave data. *J. Asian Earth Sci.*, **25**, 4, 621–628, doi: 10.1016/j.jseaes.2004.06.005.
- Hollingsworth J., Jackson J., Walker R., Gheitanchi M. R., Bolourchi M. J., 2006: Strike-slip faulting, rotation, and along-strike elongation in the Kopeh Dagh mountains, NE Iran. *Geophys. J. Int.*, **166**, 3, 1161–1177, doi: 10.1111/j.1365-246X.2006.02983.x.
- Kouhpeyma M., Talebian M., Chen L., Ghods A., Ghorashi M., 2021: Seismotectonics of the East Alborz and Kopeh-Dagh zones using local seismic network data. *Geosciences*, **31**, 1, 199–208, doi: 10.22071/GSI.2021.131130.
- Leturmy P., Robin C. (Eds.), 2010: Tectonic and stratigraphic evolution of the Zagros and Makran during the Mesozoic–Cenozoic. *Geol. Soc. Spec. Publ.*, **330**, 360 p., doi: 10.1144/SP330.0.
- Lund B., Slunga R., 1999: Stress tensor inversion using detailed microearthquake information and stability constraints: Application to Ölfus in southwest Iceland. *J. Geophys. Res. Solid Earth*, **104**, B7, 14947–14964, doi: 10.1029/1999JB900111.
- Masson F., Anvari M., Djamour Y., Walpersdorf A., Tavakoli F., Daignières M., Nankali H., Van Gorp S., 2007: Large-scale velocity field and strain tensor in Iran inferred from GPS measurements: new insight for the present-day deformation pattern within NE Iran. *Geophys. J. Int.*, **170**, 1, 436–440, doi: 10.1111/j.1365-246X.2007.03477.x.
- McClusky S., Reilinger R., Mahmoud S., Ben Sari D., Tealeb A., 2003: GPS constraints on Africa (Nubia) and Arabia plate motions. *Geophys. J. Int.*, **155**, 1, 126–138, doi: 10.1046/j.1365-246X.2003.02023.x.
- Michael A. J., 1984: Determination of stress from slip data: Faults and folds. *J. Geophys. Res. Solid Earth*, **89**, B13, 11517–11526, doi: 10.1029/JB089iB13p11517.
- Mirzaei N., Gao M., Chen Y. T., 1998: Seismic source regionalization for seismic zoning of Iran: major seismotectonic provinces. *J. Earthq. Predict. Res.*, **7**, 4, 465–495.
- Molinaro M., Guezou J. C., Leturmy P., Eshraghi S. A., Frizon de Lamotte D., 2004: The origin of changes in structural style across the Bandar Abbas syntaxis, SE Zagros (Iran). *Mar. Pet. Geol.*, **21**, 6, 735–752, doi: 10.1016/j.marpetgeo.2004.04.001.
- Regard V., Bellier O., Thomas J.-C., Abbassi M. R., Mercier J., Shabanian E., Fegghi K., Soleymani S., 2004: Accommodation of Arabia-Eurasia convergence in the Zagros-Makran transfer zone, SE Iran: A transition between collision and subduction through a young deforming system. *Tectonics*, **23**, 4, TC4007, doi: 10.1029/2003TC001599.
- Regard V., Hatzfeld D., Molinaro M., Aubourg C., Bayer R., Bellier O., Yamini-Fard F., Peyret M., Abbassi M. R., 2010: The transition between Makran subduction and the Zagros collision: recent advances in its structure and active deformation. In: Leturmy P., Robin C. (Eds.): Tectonic and stratigraphic evolution of the Zagros and Makran during the Mesozoic–Cenozoic. *Geol. Soc. Spec. Publ.*, **330**, 43–64, doi: 10.1144/SP330.4.

- Reches Z., 1987: Determination of the tectonic stress tensor from slip along faults that obey the Coulomb yield condition. *Tectonics*, **6**, 6, 849–861, doi: 10.1029/TC006i006p00849.
- Tchalenko J. S., 1975: Seismicity and structure of the Kopet Dagh (Iran, U.S.S.R.). *Philos. Trans. R. Soc. A – Math. Phys. Eng. Sci.*, **278**, 1275, 1–28, doi: 10.1098/rsta.1975.0019.
- Vavryčuk V., 2011: Principal earthquakes: Theory and observations from the 2008 West Bohemia swarm. *Earth Planet. Sci. Lett.*, **305**, 290–296, doi: 10.1016/j.epsl.2011.03.002.
- Vavryčuk V., Bouchaala F., Fischer T., 2013: High-resolution fault image from accurate locations and focal mechanisms of the 2008 swarm earthquakes in West Bohemia, Czech Republic. *Tectonophysics*, **590**, 189–195, doi: 10.1016/j.tecto.2013.01.025.
- Vavryčuk V., 2014: Iterative joint inversion for stress and fault orientations from focal mechanisms. *Geophys. J. Int.*, **199**, 1, 69–77, doi: 10.1093/gji/ggu224.
- Vernant Ph., Nilforoushan F., Hatzfeld D., Abbassi M. R., Vigny C., Masson F., Nankali H., Martinod J., Ashtiani A., Bayer R., Tavakoli F., Chéry J., 2004: Present-day crustal deformation and plate kinematics in the Middle East constrained by GPS measurements in Iran and northern Oman. *Geophys. J. Int.*, **157**, 1, 381–398, doi: 10.1111/j.1365-246X.2004.02222.x.
- Vernant Ph., Chéry J., 2006: Mechanical modelling of oblique convergence in the Zagros: Iran, *Geophys. J. Int.*, **165**, 3, 991–1002, doi: 10.1111/j.1365-246X.2006.02900.x.
- Walker R., Jackson J., 2004: Active tectonics and Late Cenozoic strain distribution in central and eastern Iran. *Tectonics*, **23**, 5, TC5010, doi: 10.1029/2003TC001529.
- Walker R. T., Bezmenov Y., Begenjev G., Carolin S., Dodds N., Gruetzner C., Jackson J. A., Mirzin R., Mousavi Z., Rhodes E. J., 2021: Slip-Rate on the Main Köpetdag (Kopeh Dagh) Strike-Slip Fault, Turkmenistan, and the Active Tectonics of the South Caspian. *Tectonics*, **40**, 8, doi: 10.1029/2021TC006846.
- Yamini-Fard F., Hatzfeld D., 2008: Seismic structure beneath Zagros-Makran transition zone (Iran) from teleseismic study: seismological evidence for underthrusting and buckling of the Arabian plate beneath central Iran. *J. Seismol. Earthq. Engng.*, **10**, 1, 11–24.
- Yamini-Fard F., Hatzfeld D., Farahbod A. M., Paul A., Mokhtari M., 2007: The diffuse transition between the Zagros continental collision and the Makran oceanic subduction (Iran): microearthquake seismicity and crustal structure. *Geophys. J. Int.*, **170**, 1, 182–194, doi: 10.1111/j.1365-246X.2006.03232.x.

Appendix

Table A1. List of focal mechanisms from the GCMT catalogue used in this study (available at www.globalcmt.org/CMTsearch.html).

Event ID	Year	Month	Day	Hour	Minute	Lon. (°E)	Lat. (°N)	Depth (km)	Mw	S1 (°)	D1 (°)	R1 (°)	S2 (°)	D2 (°)	R2 (°)	Zone
041087A	1987	04	10	6	43	57.28	37.40	15	5.1	292	45	30	180	69	131	1
020497B	1997	02	4	9	53	57.54	37.99	15	5.4	78	64	15	342	77	153	1
020497C	1997	02	4	10	37	57.50	37.82	15	6.5	328	81	-171	236	81	-9	1
020597A	1997	02	5	7	53	57.58	37.84	15	5.2	187	78	-178	97	88	-12	1
080498B	1998	08	4	11	41	57.45	37.47	15	5.3	252	84	-6	343	84	-174	1
082200D	2000	08	22	16	55	57.57	38.18	15	5.6	315	88	-179	225	89	-2	1
091900A	2000	09	19	15	19	57.44	38.08	35	5.1	40	78	-3	131	87	-168	1
201210010843A	2012	10	01	08	43	55.62	38.65	17	4.9	217	70	7	125	84	160	1
201312091133A	2013	12	09	11	33	55.67	38.68	12	5.1	209	73	16	115	74	163	1
201402130835A	2014	02	13	08	35	56.34	38.59	21	5.0	313	89	-179	223	89	-1	1
201508301438A	2015	08	30	14	38	57.84	37.00	12	4.8	333	49	126	105	52	56	1
201510122137A	2015	10	12	21	37	56.94	38.34	18	5.2	235	81	5	145	85	171	1
201605241752A	2016	05	24	17	52	57.50	37.48	18	4.8	164	79	-175	73	85	-11	1
201606292256A	2016	06	29	22	56	57.54	37.58	21	4.8	149	74	-178	59	89	-16	1
201612272056A	2016	12	27	20	56	55.76	37.04	13	4.7	271	80	-7	2	84	-170	1
201705131801A	2017	05	13	18	01	57.22	37.61	12	5.7	92	65	0	2	90	155	1
201807170358A	2018	07	17	03	58	56.96	37.26	14	4.9	187	84	-179	97	89	-6	1
202009260546A	2020	09	26	05	46	56.06	38.09	13	5.2	235	84	4	144	86	174	1
202011252011A	2020	11	25	20	11	56.03	38.12	15	4.9	140	83	174	231	84	7	1
202105162304A	2021	05	16	23	04	56.82	37.15	12	5.3	109	48	44	346	59	129	1
202105170054A	2021	05	17	00	54	56.68	37.28	12	5.5	110	35	83	299	55	95	1
081685A	2000	09	19	15	19	59.72	36.96	10	5.6	159	26	162	265	82	65	2
112792H	1992	11	27	21	09	59.77	37.36	24	5.3	166	68	172	259	82	22	2
121494E	1994	12	14	20	43	58.66	35.56	33	5.2	319	32	144	80	72	63	2
110899G	1999	11	8	21	37	61.38	36.04	44	5.5	304	43	88	126	47	92	2
110999A	1999	11	9	5	20	61.29	35.78	25	5.3	160	5	89	342	85	90	2
110999D	1999	11	9	11	49	61.19	35.90	23	4.9	162	43	67	13	51	110	2
120599C	1999	12	5	13	12	61.50	35.91	20	4.9	107	41	112	259	53	72	2
070303E	2003	07	3	14	59	60.84	35.66	30	5.1	316	30	109	114	62	79	2
201201191235A	2012	01	19	12	35	58.90	36.27	20	5.3	292	24	80	123	66	94	2
201704050609A	2017	04	05	06	09	60.37	35.81	12	6.0	91	44	59	312	53	117	2
201704052007A	2017	04	05	20	07	60.40	35.84	17	5.0	307	47	143	64	64	50	2
201705022112A	2017	05	02	21	12	60.58	35.66	12	5.1	102	39	43	336	64	121	2
120979A	1979	12	9	9	12	56.60	34.80	15	5.6	350	44	121	129	53	63	3

Table A1. Continued from the previous page.

Event ID	Year	Month	Day	Hour	Minute	Lon. (°E)	Lat. (°N)	Depth (km)	Mw	S1 (°)	D1 (°)	R1 (°)	S2 (°)	D2 (°)	R2 (°)	Zone
121494E	1994	12	14	20	43	58.66	35.56	33	5.2	319	32	144	80	72	63	3
022596H	1996	02	25	16	14	57.35	35.65	33	5.4	82	77	10	350	80	166	3
022596I	1996	02	25	17	42	57.22	35.85	33	5.3	257	79	5	166	85	169	3
020200C	2000	02	2	22	58	58.19	35.46	27	5.3	83	43	79	278	48	100	3
200505310838A	2005	05	31	08	38	57.75	34.73	25	4.7	309	84	-1	39	89	-174	3
200807032310A	2008	07	03	23	10	58.60	35.50	12	5.1	310	42	101	116	49	81	3
201007301350A	2010	07	30	13	50	59.36	35.17	28	5.5	188	57	155	292	70	36	3
201704050609A	2017	04	05	06	09	56.60	34.80	15	5.6	350	44	121	129	53	63	3
201505052128A	2015	05	05	21	28	58.32	35.33	34	5.1	275	67	-16	11	75	-157	3
201610251158A	2016	10	25	11	58	56.97	35.45	9	4.1	174	77	-172	82	82	-13	3
201908132331A	2019	08	13	23	31	56.54	34.93	15	4.0	153	87	171	244	81	3	3
121977B	1977	12	19	23	34	56.25	30.61	24	5.9	231	69	4	140	86	159	4
052278A	1978	05	22	6	18	55.73	31.25	15	5.1	144	65	155	246	67	28	4
091678B	1978	09	16	15	35	57.02	33.37	11	7.3	328	33	107	128	59	80	4
021379B	1979	02	13	10	36	57.31	32.99	15	5.5	331	39	114	121	55	71	4
011280A	1980	01	12	15	31	56.93	33.24	15	6.0	356	23	145	118	77	71	4
072881A	1981	07	28	17	22	57.58	30.03	15	7.2	150	13	119	300	79	84	4
080684A	1984	08	6	11	14	56.92	30.84	19	5.4	72	39	66	282	55	109	4
112089A	1989	11	20	4	19	57.80	29.89	15	5.9	240	75	9	148	81	165	4
032590A	1990	03	25	0	01	56.99	33.34	15	5.1	223	90	-180	313	90	0	4
101590C	1990	10	15	19	06	56.74	33.56	15	5.1	114	45	58	335	53	118	4
031498F	1998	03	14	19	40	57.60	29.95	15	6.6	154	57	-174	61	85	-33	4
111898A	1998	11	18	7	39	57.38	30.26	15	5.3	174	55	173	268	85	35	4
040502C	2002	04	5	18	40	56.07	31.85	33	5.2	65	72	4	334	86	162	4
101602C	2002	10	16	9	20	56.23	31.19	33	5.3	298	37	176	31	88	53	4
200502220225A	2005	02	22	02	25	56.81	30.76	12	6.4	71	44	79	266	47	100	4
200505011858A	2005	05	01	18	58	56.93	30.64	20	5.1	214	63	3	122	87	153	4
200505141804A	2005	05	14	18	04	56.84	30.72	12	5.2	69	53	46	307	55	133	4
200506190446A	2005	06	19	04	46	58.03	33.06	13	4.9	112	52	33	1	65	137	4
200605070620A	2006	05	07	06	20	56.69	30.79	12	5.0	324	72	-162	228	73	-19	4
200707040611A	2007	07	04	06	11	55.96	32.16	12	5.0	330	63	176	62	87	27	4
201106261947A	2011	06	26	19	47	57.57	29.89	22	5.1	114	36	71	317	56	103	4
201202271848A	2012	02	27	18	48	56.73	31.35	12	5.2	89	40	59	307	57	113	4
201212031253A	2012	12	03	12	53	57.35	30.36	22	4.8	305	38	135	73	64	61	4
201301211949A	2013	01	21	19	49	57.41	30.23	12	5.3	235	70	13	141	78	160	4
201308272200A	2013	08	27	22	00	56.44	32.51	26	4.9	354	54	154	99	70	39	4
201507251610A	2015	07	25	16	10	57.51	29.89	22	4.8	73	65	11	338	80	154	4

Table A1. Continued from the previous page.

Event ID	Year	Month	Day	Hour	Minute	Lon. (°E)	Lat. (°N)	Depth (km)	Mw	S1 (°)	D1 (°)	R1 (°)	S2 (°)	D2 (°)	R2 (°)	Zone
201507311006A	2015	07	31	10	06	57.51	29.94	24	5.4	156	82	180	246	90	8	4
201610201510A	2016	10	20	15	10	56.46	30.72	15	4.8	229	40	10	131	84	129	4
201707231732A	2017	07	23	17	32	57.45	30.01	18	5.2	333	76	180	63	90	14	4
201712010232A	2017	12	01	02	32	57.16	30.64	12	6.1	120	29	81	310	61	95	4
201712010335A	2017	12	01	03	35	57.27	30.61	12	5.4	83	43	23	336	75	130	4
201712021047A	2017	12	02	10	47	57.19	30.66	12	5.1	85	41	38	325	66	125	4
201712120843A	2017	12	12	08	43	57.10	30.66	12	6.0	123	26	85	309	64	92	4
201712122141A	2017	12	12	21	41	57.13	30.74	12	6.0	112	31	94	287	59	87	4
201712211704A	2017	12	21	17	04	56.22	31.29	15	5.2	336	59	-175	244	86	-31	4
201712271801A	2017	12	27	18	01	57.17	30.63	20	4.9	104	43	42	341	63	125	4
201801110318A	2018	01	11	03	18	57.41	30.64	18	4.9	267	46	107	63	46	73	4
201801111335A	2018	01	11	13	35	57.17	30.59	12	5.0	100	44	40	339	64	126	4
201807222039A	2018	07	22	20	39	57.44	30.22	15	5.5	147	78	180	237	90	12	4
202002240033A	2020	02	24	00	33	56.64	31.16	22	4.8	215	74	16	120	75	164	4
202010262134A	2020	10	26	21	34	55.90	32.17	17	4.9	151	51	156	257	71	42	4
110776A	1976	11	7	4	00	59.15	34.07	15	6.0	260	78	6	169	84	168	5
011679A	1979	01	16	9	50	59.41	34.19	15	6.5	267	49	5	174	86	139	5
111479A	1979	11	14	2	21	59.78	34.37	12	6.5	256	53	-1	347	89	-143	5
112779B	1979	11	27	17	10	59.58	34.45	25	7.0	261	67	-19	358	73	-156	5
120779A	1979	12	7	9	24	59.52	33.96	15	6.1	105	76	-1	195	89	-166	5
112487E	1987	11	24	11	23	58.98	32.23	15	5.3	144	39	106	303	53	77	5
031590A	1990	03	15	0	12	60.30	31.44	15	5.1	100	82	-1	190	89	-172	5
051097C	1997	05	10	7	57	60.02	33.58	15	7.2	248	83	0	338	90	-173	5
061697A	1997	06	16	3	00	60.07	33.29	15	5.0	151	36	131	284	64	64	5
062097B	1997	06	20	12	57	59.97	32.19	15	5.5	189	87	-179	99	89	-3	5
062597G	1997	06	25	19	38	59.43	34.04	15	5.8	180	71	169	273	79	19	5
041098C	1998	04	10	15	00	60.10	32.35	33	5.7	263	77	9	171	81	167	5
102300B	2000	10	23	6	54	59.33	31.93	33	5.2	92	40	24	343	75	128	5
112103C	2003	11	21	10	34	58.95	31.11	33	5.0	98	40	40	335	66	123	5
200803090351A	2008	03	09	03	51	59.17	33.25	12	5.0	338	75	172	70	82	15	5
201111210156A	2011	11	21	01	56	59.92	32.05	13	5.0	101	43	43	336	62	124	5
201207012201A	2012	07	01	22	01	59.94	34.51	21	5.2	168	30	114	321	62	77	5
201209020050A	2012	09	02	00	50	60.04	33.35	21	5.0	108	39	59	325	58	112	5
201212051708A	2012	12	05	17	08	59.60	33.41	15	5.8	92	45	19	348	76	133	5
202001020429A	2020	01	02	04	29	60.26	34.02	15	5.5	82	73	13	347	77	162	5

Lon. – longitude, Lat. – latitude, Mw – moment magnitude, S1/S2, D1/D2, R1/R2 – strike, dip and rake for two conjugate solutions